ADVANCED FUNCTIONAL MATERIALS
www.afm-journal.de

Porous Silicon Resonant Microcavity Biosensor for Matrix Metalloproteinase Detection

*Fransiska S. H. Krismastuti, Stephanie Pace, and Nicolas H. Voelcker**

A real-time, sensitive, and selective detection device to monitor the healing status of chronic wounds at the point of care is urgently required to render the management of this disease more effective. The photonic properties of porous silicon resonant microcavity (pSiRM) afford an excellent opportunity to be developed as a highly sensitive optical biosensor to monitor the presence of specific biomarkers found in the wound exudate, such as matrix metalloproteinases (MMPs). In this study, the pSiRM is designed, fabricated, and functionalized using a fluorogenic MMP peptide substrate featuring both a fluorophore and a quencher. The peptide-functionalized pSiRM is then employed as a fluorescence-based optical biosensor for MMPs. Active MMPs recognize and cleave the peptide sequence of the substrate, producing an immobilized peptide fragment carrying the fluorophore. The fluorescence intensity of the fluorophore embedded within the pSiRM matrix is enhanced by the photonic structure of the pSiRM compared to other pSi photonic structures. This fluorescence enhancement translates into high sensitivity, enabling detection of MMP-1 at a limit of detection as low as 7.5×10^{-19} M after only 15 min incubation time. Finally, the biosensor also allows the detection and quantification of the concentration of MMPs in human wound fluid.

1. Introduction

The management of chronic wounds such as diabetic foot ulcers, pressure ulcers and venous leg ulcers is lengthy and challenging due to the inherent complexity of the biochemical processes occurring in non-healing wounds. Regular examinations and assessments of the wound bed need to be performed by nurses and clinicians to inform the individual patient's wound treatment plan.[1] This assessment process consumes a significant amount of nursing time and dressing materials, which contribute to spiraling medical costs in wound care.[2] In order to make inroads to improve chronic wound management, the development of diagnostic tools that provide fast, sensitive, selective and low-cost detection of biomarkers of wound healing status is highly desirable, particularly considering the increasing prevalence of chronic wounds in ageing societies around the world.[3–5]

F. S. H. Krismastuti, Dr. S. Pace, Prof. N. H. Voelcker
Mawson Institute
University of South Australia
Adelaide, South Australia 5095, Australia
E-mail: nico.voelcker@unisa.edu.au

DOI: 10.1002/adfm.201304053

The deployment of advanced detection technologies, such as diagnostic and theranostic sensors in the wound management, especially for monitoring the healing status of acute and chronic wounds is rapidly growing.[2,6] The ideal diagnostic tool would afford a clear and simple read-out, not requiring interpretation from medical expert, while a theranostic would release therapeutics in response to altered wound healing,[1,2,6] for instance as a result of bacterial infection.[7–9] It would be desirable for such diagnostic or theranostic sensors to be incorporated into a wound dressing (a "smart" dressing) or deployed as a point-of-care (POC) device that provides fast responsive and is both sensitive and selective.

Given the complexity of wound healing and the wound exudate matrix, a plethora of molecules have been identified as wound biomarkers, as listed by Harding et al.[1] However, a clinically validated biomarker in chronic wounds is in the group of matrix metalloproteinases (MMPs).[1,2,10,11] MMPs are proteolytic enzymes involved in the extracellular matrix (ECM) degradation and tissue remodeling processes during wound healing.[11–13] There are more than 20 MMPs which contain at least ≈20 amino acid residue long signal peptides.[12] In general, MMPs can be classified into five groups based on their structural and functional properties. Those are the collagenases (such as MMP-1 and MMP-8); the gelatinases (including gelatinase-A or MMP-2); the stromelysins (such as stromelysin-1 or MMP-3); the membrane-type MMPs (such as MT1-MMP or MMP-14) and the heterogeneous subgroup containing matrilysin (MMP-7), enamelysin (MMP-20), and macrophage metalloelastase (MMP-12).[12,14,15]

The activity of MMPs can be inhibited by tissue inhibitors of metalloproteinases (TIMPs)[12,14–17] or synthetic inhibitors.[12,16] The inhibition involves forming a chelate complex between TIMPs and a zinc ion at the active site of MMP.[11,16] This affords the possibilities of a therapeutic intervention by administration of synthetic MMP inhibitors to maintain the level of MMPs and promote wound healing.[11,18] However, the concentration of MMPs needs to be known to correctly dose the inhibitor since over-inhibition is also deleterious.[11] Therefore, chronic wound management would benefit from a POC sensor that is able to rapidly establish MMP levels in wound fluid.

MMPs assays already exist, but they have not been developed and demonstrated for chronic wounds.[19–21] For example, Beekman et al.[19] synthesized a soluble and selective fluorogenic peptide substrate TNO211 (Dabcyl-Gaba-Pro-Gln-Gly-Leu-Glu(EDANS)-Ala-Lys-NH_2) containing an MMP cleavable peptide sequence (Gly-Leu) and a pair of EDANS (5-((2-aminoethyl)amino)naphthalene-1-sulfonic acid) and Dabcyl (4-(4-dimethylaminophenylazo)benzoyl) as fluorophore and quencher, respectively. Using this substrate, they were able to detect MMPs in complex samples, such as a culture media and synovial fluid.[19] This particular peptide substrate is now commercially available (produced by Merck and known as MMP substrate III, fluorogenic).

There are four examples where porous silicon (pSi) was used in the design of MMP sensors.[20–23] Gao et al.[20] achieved MMP-2 detection as low as 1.5×10^{-12} M. The sensor was based on a pSi rugate filter coated with gelatin, which can be digested by MMP-2. The digestion products then entered to the pSi matrix and induced color changes that could be observed by naked eyes. Martin et al.[21] designed a biosensor to detect MMP-8 based on antibody-functionalized pSiRM and monitored the presence of MMP-8 by observing the shift in the resonance cavity dip of the pSiRM. This device was able to detect MMP-8 down to 1.5×10^{-9} M. However, both sensors did not demonstrate operation in complex biological fluids. A MMP sensor that was able to detect MMP secreted by living cells was studied by Kilian et al.[22] They developed a label-free sensor to detect MMPs secreted by human macrophages as an example of biological fluid. The sensor was based on photonic crystals of pSi filled with gelatin. It successfully detected MMP-9 as low as 1.2×10^{-12} M. In our previous study, we developed an optical biosensor based on single layer pSi functionalized with a synthetic MMP inhibitor and demonstrated that the sensor selectively detected the MMPs in wound fluid sample at physiologically concentrations of MMPs found in chronic wound fluid.[23]

The above examples relied on pSi since this material holds significant potential for label-free optical biosensors because of its very large surface area (up to 600 $m^2\ g^{-1}$), tunable morphological and optical properties, biocompatibility and versatile surface chemistry.[24] Pore size can be tuned to allow ingress of even large biomolecules such as antibodies.[25] The electrochemical anodization procedure allows the generation of diverse pSi architectures such as single layers, multilayers (Bragg reflectors and rugate filters) as well as resonant microcavities.[24] The morphological properties such as pore size, porosity and thickness can be tuned to fabricate pSi structure suitable for ingress of the targeted biomolecule while excluding others.[25,26] Biocompatibility of the sensor material is essential when direct contact of the sensor with human body, such as through a smart dressing.[26] pSi is well tolerated in vitro and in vivo and degrades into orthosilicic acid, the natural form of silicon in humans.[27,28] The pSi surface can be modified in order to increase the stability of the material in aqueous milieu and immobilize biorecognition molecules.[29–31]

The pSiRM is a photonic structure consists of two distributed Bragg reflectors (DBR) separated by a cavity layer, producing a reflectance spectrum with a sharp resonance cavity dip in the center of the reflectance band.[32–34] Each DBR consists of periodical layers of alternating low porosity (LP) and high porosity (HP) pSi, with high and low refractive index, respectively, but the same optical thickness. The optical thickness for each DBR is $\lambda/4$, where λ is the central wavelength of the photonic resonance band with near 100% reflectance. The resonance cavity is built with an optical thickness of an integer multiple of $\lambda/2$. The position of the central wavelength of the resonance cavity dip is easily tuned by changing the electrochemical etching parameters.[35]

The pSiRM has two interesting optical features for biosensing applications. Firstly, the resonance cavity dip of the pSiRM is sensitive to the refractive index changes.[20] The small refractive index change induces a large shift of the optical spectrum.[21,25,36–40] This optical feature lends itself to biosensor design and has been previously explored in biosensing applications, such as glucose detection,[35] bacteria detection,[33,41] viruses and DNA detection.[42] The second optical feature is a confinement effect of light inside the cavity layer to specific wavelength contributing to the enhancement of fluorescence emission of fluorophore immobilized on the pSiRM matrix as recently studied by Sciacca et al.[43] and Palestino et al.[37] The optimum enhancement of the fluorescence emission is obtained if the wavelength of the microcavity dip is aligned with the emission wavelength of the fluorophore.[43]

In this study, we developed an optical biosensor based on the photonic structure of pSiRM functionalized using the fluorogenic MMP peptide substrate, Dabcyl-Gaba-Pro-Gln-Gly-Leu-Glu(EDANS)-Ala-Lys-NH_2. In the presence of MMPs, the peptide fragment carrying the quencher was cleaved off the surface, which allowed the EDANS fluorescence emission to be activated. In particular study, we targeted MMP-1 as one of collagenases because this enzyme is one of key enzymes responsible for cleaving interstitial fibrillar collagen[44] which is very crucial during wound healing.[45] We confirmed that the pSiRM structure afforded enhanced emission in comparison to other pSi structures and allowed detection of MMP-1 down to the attomolar level in buffer. This pSi optical biosensor was also successfully applied to detect MMPs in human wound fluid.

2. Results and Discussion

2.1. Design, Fabrication, and Characterization of the pSiRM as an Optical Biosensor Platform

The optical biosensor investigated in this study was based on a photonic pSiRM which consisted of two DBR and one resonance cavity layer. Each DBR had a periodic layer structure alternating between different porosities (HP and LP) with a quarter-wavelength ($\lambda/4$) optical thickness while the defect layer had a HP layer with an optical thickness of a multiple of half-wavelength ($\lambda/2$). The first task was to design a pSiRM with appropriate porosity contrast between HP and LP layers. We therefore prepared five single layer pSi samples etched at different current densities for 120 s. The samples were characterized morphologically and optically to determine pore size, porosity and thickness (see Supporting Information, Table S1).

The average pore diameters and thickness were measured by means of scanning electron microscopy (SEM) (see Supporting Information, Figure S1). The porosity and the thickness values

were determined using interferometric reflectance spectroscopy (IRS) and a simulation using the transfer matrix method. The thickness values obtained from the simulation were in good agreement with the SEM result. The fringe patterns obtained for the single layer pSi samples are a result of Fabry-Pérot interferences and obey the equation:[24,46,47]

$$m\lambda = 2nL \quad (1)$$

where m is the fringe order, λ is the wavelength of the incident light for maximum constructive interferences, n is the refractive index of the porous film, L is the film thickness and the factor of 2 is derived from the factor of 90° backscatter configuration of the light source and detector.[46,48] The optical thickness of the film, the product of refractive index and film thickness can be determined from the reflectance spectrum by applying a fast Fourier transform (FFT).[48] The transfer matrix method was used to obtain the best fit between the experimental and the theoretical reflectance spectra over the spectrometer's wavelength range by adjusting the porosity and thickness parameters. Table S1 (Supporting Information) shows that the pore diameter, porosity and thickness increased as the etching current density increased, as expected. The etching rate was calculated by dividing the thickness over the etching time.

Since we targeted MMPs and in particular MMP-1 which has a molecular weight of 42 kDa and unit cell dimensions of approximately of 14 nm × 14 nm × 11 nm,[44] a mesoporous pSiRM with pores >30 nm was required to allow MMP-1 ingress throughout the structure. This was achieved for all five etching conditions in Table S1. Once porosity, etching rate and pore size were determined for each current density profile, the pSiRM could be designed and simulated using the transfer matrix method.[46] The mesoporous pSiRM used in this study was designed with a symmetric mirror and a configuration of $(HP/LP)_3(HP)_4(LP/HP)_3$. Each DBR featured three periodic bilayers with a porosity of 83.4% for HP and a porosity of 67.0% for LP starting with HP for the first DBR and LP for the second DBR. Those porosity values produce pore diameters ranging from 40–60 nm for LP layer and 110–140 nm for HP layer, respectively. Those pore sizes were large enough to allow ingress of the desired target molecules while retaining the sensitivity of the biosensor. The pore size is an important parameter because it affects the internal surface area of the pSiRM where the biorecognition molecules are attached and the target analyte is captured.[25,36] By decreasing the pore size, the internal surface area and the density of available binding sites for target molecules are increased, which translates into higher sensitivity.[40] On the other hand, too small pore sizes prevent infiltration of large biomolecules into the entire porous layers.[25,36] The chosen parameters therefore represent a compromise between these two requirements.

We observed that the surface modification of the pSiRM influenced the position of the microcavity dip, requiring an adjustment of the etching conditions to compensate for those effect and achieve good alignment between the resonance cavity dip and the maximum fluorescence emission peak of the chosen fluorophore (in this case with EDANS at 446.5 nm). The good alignment between them leads to the enhancement effects of fluorescence emission of the fluorophore in the pSiRM structure, which is key to sensitive MMP detection. The surface modification steps shifted the resonance cavity dip 6.5 nm towards longer wavelength (red shift) and this shift will be explained in the next section. In order to compensate for the shift due to surface modification and produce the resonance cavity dip at 446.5 nm after surface modification, in this study, the pSiRM was designed with a center wavelength (λ) of the resonance cavity dip at 440 nm measured at a light incidence angle of 36° or at 478 nm at 0° (a 38 nm blue shift from the angle of 0° to 36°). However, the experimental result obtained by IRS also showed that the pSiRM designed at 440 nm produced the resonance cavity dip at 448 nm (at an angle of 36°) corresponding to an 8 nm red shift different between design and the IRS experiment (**Figure 1**a). Therefore, to compensate for this shift and indeed produce the resonance cavity dip at 440 nm after etching or 446.5 nm after surface modification, as required for maximum overlap with EDANS emission, the pSiRM was re-designed at 432 nm. In this design, the refractive indices (n) were 1.3 and 1.8 for the HP and LP layer, respectively, calculated using Bruggeman effective medium approximation. The value of n and λ were used to determine the thickness of each periodic layer considering the $\lambda/4$ for each DBR and $\lambda/2$ for the defect layer. During the fabrication of the pSiRM, the HP layer formed an 83 nm thick layer, while the LP layer formed a 60 nm thickness. It should be noted that the thickness values obtained from the simulation were in good agreement with the values obtained from SEM cross-sections of the produced pSiRM.

The surface was also characterized by SEM (Figure 1b,c) to obtain the top-view and cross-section images of the pSiRM. Figure 1b shows the top view SEM image of mesoporous pSiRM with the pore sizes ranged from 110–140 nm representing the pore size of the top layer of the DBR or in this case is the HP layer. The cross-sectional SEM image in Figure 1c reveals the periodic layers forming the pSiRM, with the top and bottom DBR each featuring 3 periodic layers of HP/LP separated by an HP resonance cavity layer. The thickness of the periodic layer of the pSiRM was 1.19 µm.

2.2. Surface Functionalization of the pSiRM

The freshly etched pSiRM features a hydride-terminated surface. This surface is unstable and tends to oxidize in the presence of oxygen or to hydrolyze in the presence of water leading to uncontrollable optical properties which is undesirable for biosensor applications.[29,31,49] Here, we functionalized the pSiRM surface by means of hydrosilylation of undecylenic acid. This chemistry produces a dense alkyl monolayer with stable Si-C bonds protecting the pSiRM surface from oxidative hydrolysis.[49,50] The carboxylic acid can then be converted into a succinimidyl ester which reacts readily with the amine group of the fluorogenic MMP peptide substrate, as shown in **Figure 2**a.

The pSiRM samples were characterized by Fourier transform infrared (FTIR) spectroscopy in the attenuated total reflectance (ATR) mode after every surface functionalization step (Figure 2b). Hydrosilylation of the freshly etched pSiRM surface using neat undecylenic acid (Spectrum (i)) replaced the Si–H bonds on the surface with Si–C bonds. This was confirmed by

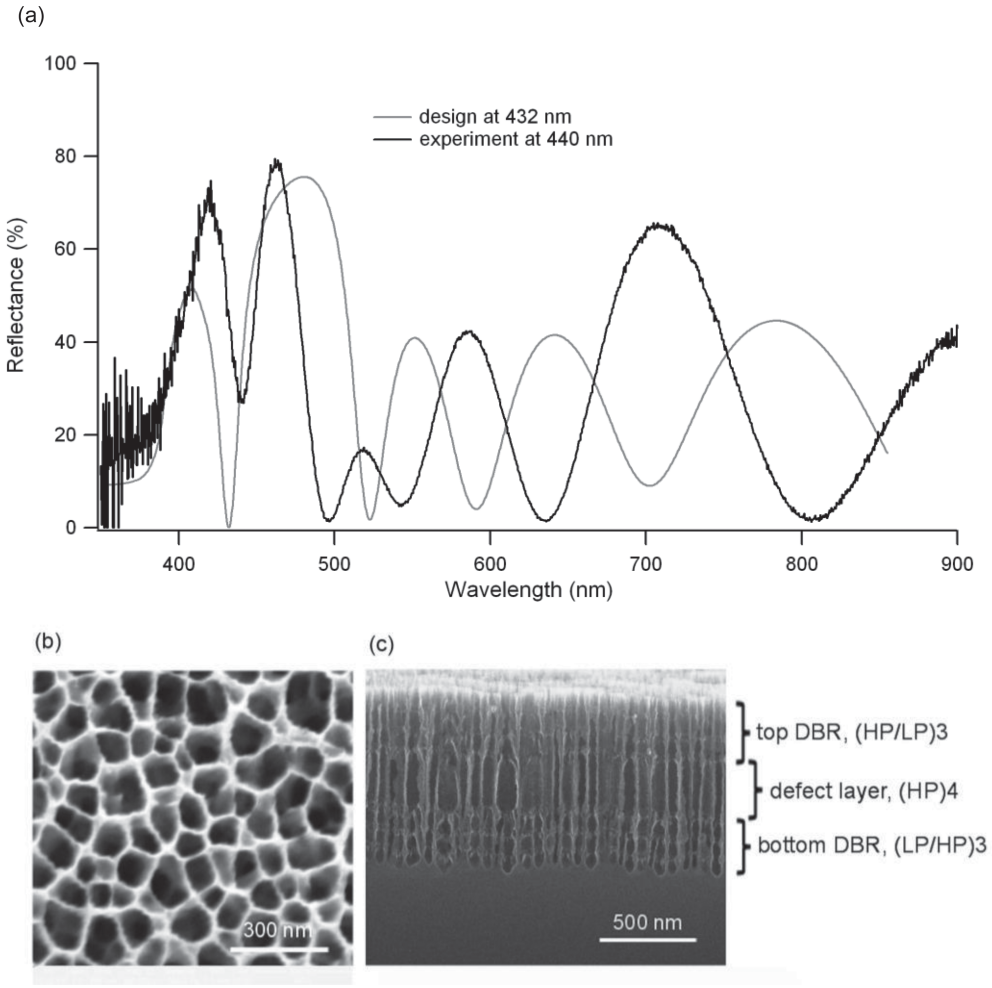

Figure 1. Characterization of the pSiRM structure with a configuration of $(HP/LP)_3(HP)_4(LP/HP)_3$. a) Simulated reflectance spectrum of pSiRM (grey trace) and reflectance spectrum obtained using IRS from a freshly etched pSiRM (black trace). b) Top view and c) cross-sectional SEM images of the freshly etched pSiRM.

the appearance of characteristic bands at 1459 cm^{-1}, 2865 cm^{-1} and 2935 cm^{-1} which were assigned to the $\Delta_{CHtet.}$ deformation mode of methylenes and the stretching vibrational of aliphatic C–H bonds, respectively. The characteristic band of $\nu_{(C=O)}$ stretching mode of a carboxylic acid was observed at 1714 cm^{-1}. The presence of very faint bands at 904 cm^{-1} and 2100 cm^{-1}, assigned to $Si–H_2$ scissor vibrational mode and $Si–H_x$ stretching vibrational mode of the freshly etched pSi, respectively, indicate that there is a small amount of unreacted silicon hydride groups left on the surface. In addition, the band at 1033 cm^{-1} attributed to the Si–O stretching vibrational indicates the presence of silicon dioxide at the surface of the pSiRM. Residual silicon hydrides and a small amount of surface oxidation are commonly observed in the hydrosilylation of pSi.[49–52]

The activation of a grafted acid-terminated layer with EDC in the presence of NHS (Spectrum (ii)) resulted in further spectral changes including a triplet band at 1735 cm^{-1}, 1785 cm^{-1}, and 1815 cm^{-1} which is characteristic for the formation of the NHS ester group.[49–51] The bands at 1735 cm^{-1} and 1785 cm^{-1} were assigned to the $\nu_{as(C=O)}$ antisymmetric stretching vibrational mode and to the $\nu_{s(C=O)}$ symmetric stretching vibration of the succinimidyl cycle, respectively, while the band at 1815 cm^{-1} was assigned to two distinct chemical species, the $\nu_{s(C=O)}$ symmetric stretching vibrational mode and the $\nu_{(C=O)}$ stretching vibrational mode of the succinimidyl ester carbonyl.[49,51] After immobilization of the fluorogenic substrate, bands at 1660 cm^{-1} and 1554 cm^{-1} (Spectrum (iii)) appeared that were attributed to the amide I and amide II bonds. The presence of those bands gave a strong indication that the peptide was covalently bound to the pSiRM surface via amide bonds.[49]

These surface reactions were also followed using IRS to study the effects on the optical properties of the pSiRM and in particular on the wavelength shift of the microcavity dip.[25] A red shift of 5 nm was observed after the hydrosilylation reaction, followed by a red shift after activation with succinimidyl ester ($\Delta\lambda$ = 1 nm) and then another red shift after immobilisation of the fluorogenic substrate ($\Delta\lambda$ = 1 nm). A small blue shift ($\Delta\lambda$ = 0.5 nm) was observed after incubation with MMP-1. Thus, overall the surface modification gave a total 6.5 nm red shift. These shifts needed to be considered when designing the wavelength position of resonance dip of the pSiRM, as explained in the previous section.

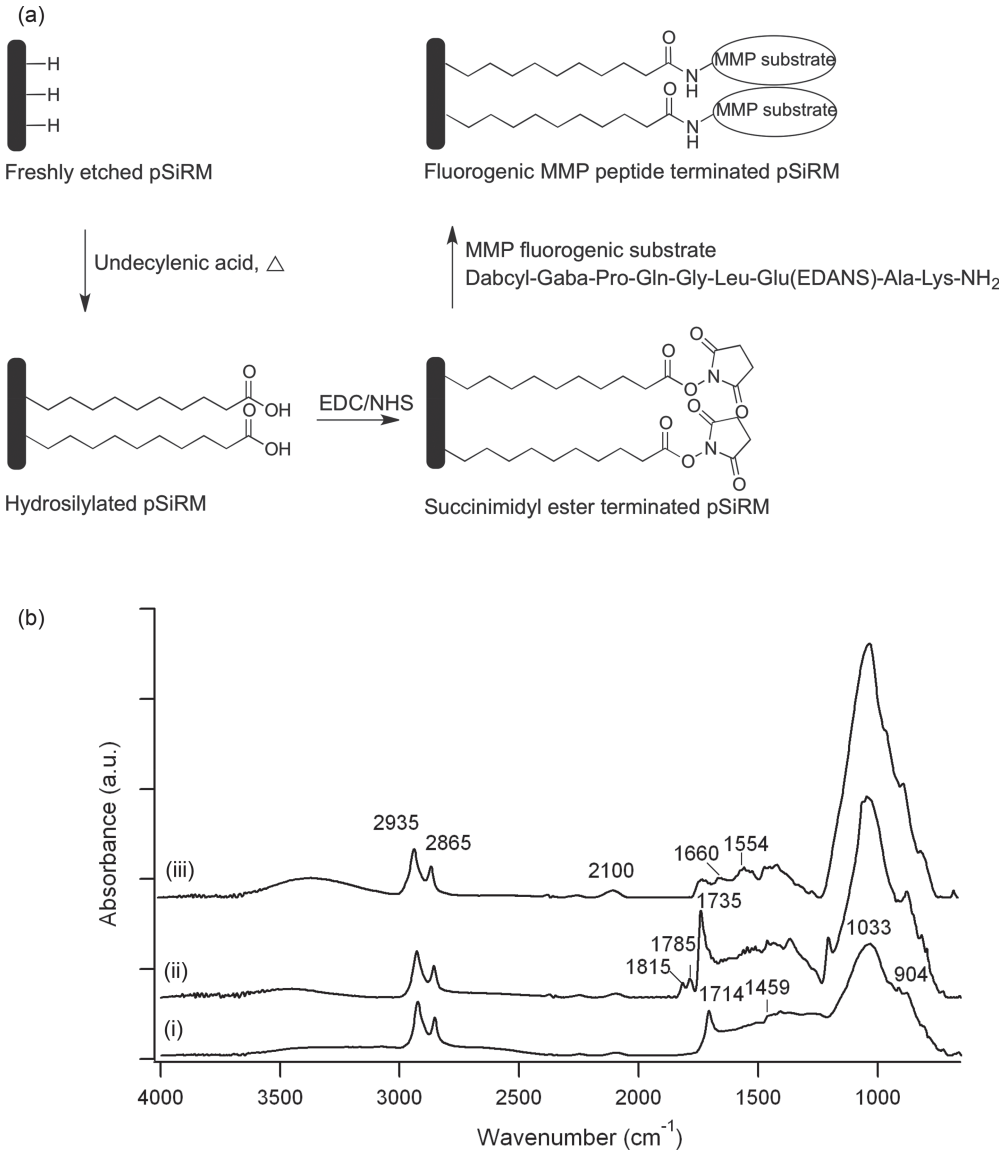

Figure 2. a) Surface functionalization reactions of the hydride-terminated pSiRM surface involving hydrosilylation with undecylenic acid, NHS ester formation and reaction with fluorogenic MMP substrate. b) The baseline-corrected of FTIR-ATR spectra of the pSiRM surface i) after hydrosilylation with undecylenic acid, ii) activation with EDC/NHS. and iii) immobilization of the fluorogenic MMP peptide substrate.

The 5 nm red shift after hydrosilylation can be explained by an increase in effective refractive index due to the monolayer formation of undecylenic acid within the porous layer and is consistent with what other groups have observed. For example, Ouyang et al. observed the shift of microcavity dip after binding of thin layer molecules with different thickness considering some parameters, such as pore diameter and the refractive index changes before and after binding. They reported that a 10 nm red shift of the resonance cavity dip in the macroporous microcavity was produced by a 3 nm thick coating, which means, in our case, that for a 5 nm red shift, the monolayer thickness should be 1.5 nm.[25] This thickness is in reasonable agreement with what Böcking et al. observed for an undecylenic acid monolayer using X-ray reflectometry (0.9–1.1 nm).[53]

2.3. MMP-1 Detection using the pSiRM Optical Biosensor

2.3.1. Sensing Principle

The peptide-functionalized pSiRM was then used to detect MMP-1 in buffer solution. MMP-1 was chosen since this MMP is prominent in wound fluid[54,55] and is known to cleave the fluorogenic peptide sequence.[19] The sensing was performed by incubating the peptide-functionalized pSiRM in the MMP-1 solution. The pSiRM was then rinsed and dried for measurement. A small blue shift ($\Delta\lambda$ = 0.5 nm) observed by IRS after incubation with MMP-1 on the pSiRM gave a first indication that the peptide was indeed cleaved in the presence of MMPs. However, this small shift would limit the sensitivity of the device if the sensing was only done by IRS. Thus, we focused

on an alternative approach to detect the MMP-1, exploiting fluorescence enhancement effects in the pSiRM structure.

2.3.2. MMP-1 Biosensing Experiments

The peptide-functionalized pSiRM in the absence of MMP-1 did not show any fluorescence at 446.5 nm, demonstrating that the Dabcyl moiety effectively quenched the EDANS fluorescence in the intact peptide (**Figure 3**a). However, when the pSiRM was incubated with an MMP-1 containing solution for a few minutes, emission at 446.5 nm was observed, indicating that MMP-1 had indeed cleaved the peptide and removed the quencher. This result demonstrates that the immobilization of the fluorogenic MMP peptide substrate into the pSiRM matrix did not prevent digestion by MMP-1. The fluorescence spectra generated from the pSiRM samples after MMP-1 incubation were compared with the fluorescence signal of the fluorogenic substrate in the buffer solution at the same incubation time and MMP-1 concentration (Figure 3a–c). The comparison shows that the emission peak of the fluorophore in the solution (FWHM ≈ 87 nm) was about ten times broader than the emission peak of the fluorophore attached on the pSiRM surface (FWHM ≈ 8 nm). This conspicuous difference is testament to the effect of the pSiRM structure in confining the width of the wavelength band that escapes the microcavity. In addition, the fluorescence intensity of the fluorophore embedded in the pSi matrix was higher than the fluorescence intensity of the fluorophore in the solution at the same MMP-1 concentration. We attribute this effect to the fluorescence enhancement of the microcavity.[37,43,56] The larger error bars for the pSiRM compared to the solution measurement are probably due to slight variations in the surface concentration of the immobilized peptide for each sample.

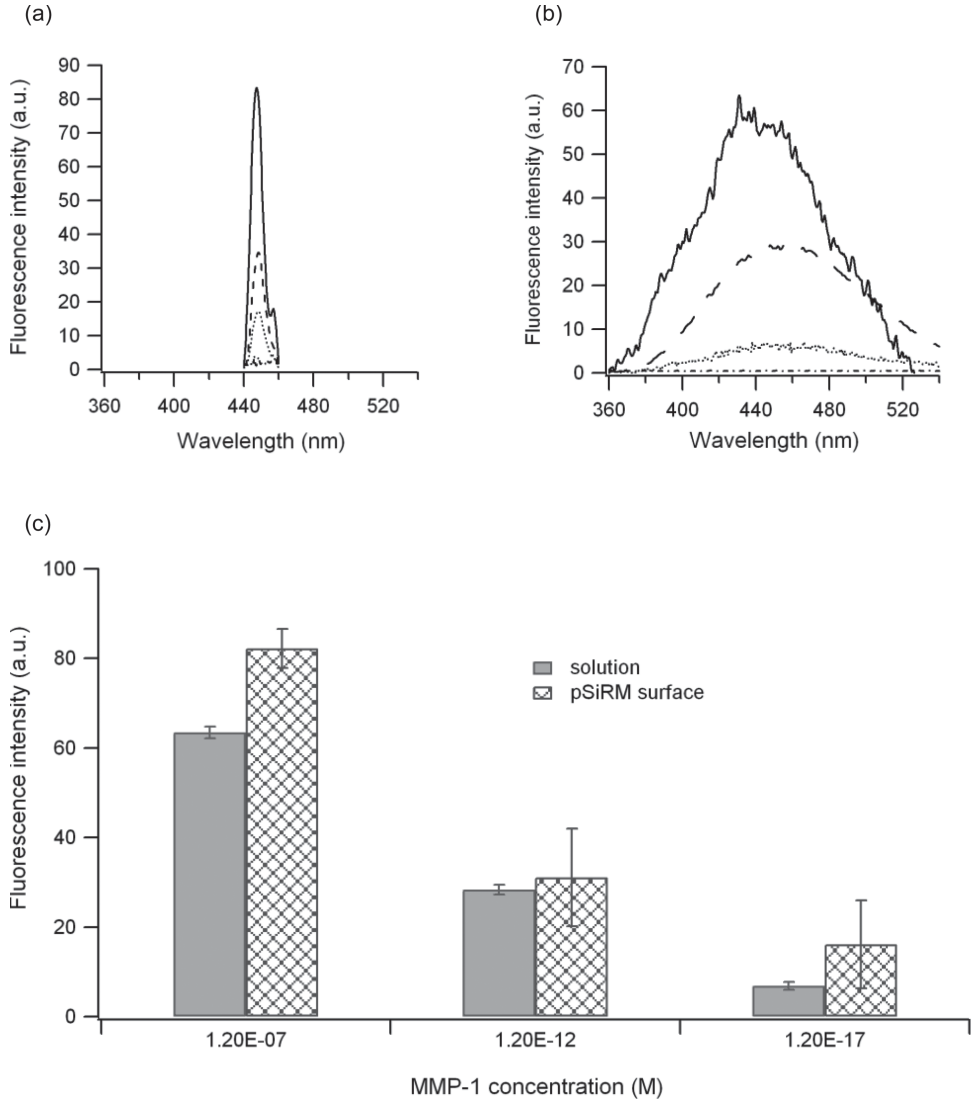

Figure 3. EDANS emission spectra immobilized a) in the pSiRM matrix and b) in buffer solution from 3 different MMP-1 concentrations: 1.2×10^{-7} M (full line); 1.2×10^{-12} M (dashed line); 1.2×10^{-17} M (dotted line); and 0 M (dot and dashed line). c) Emission intensity at 446.5 nm for each concentration of MMP-1 in the buffer solution (solid) and on the pSiRM surface (pattern), with the error bars calculated from three separate experiments.

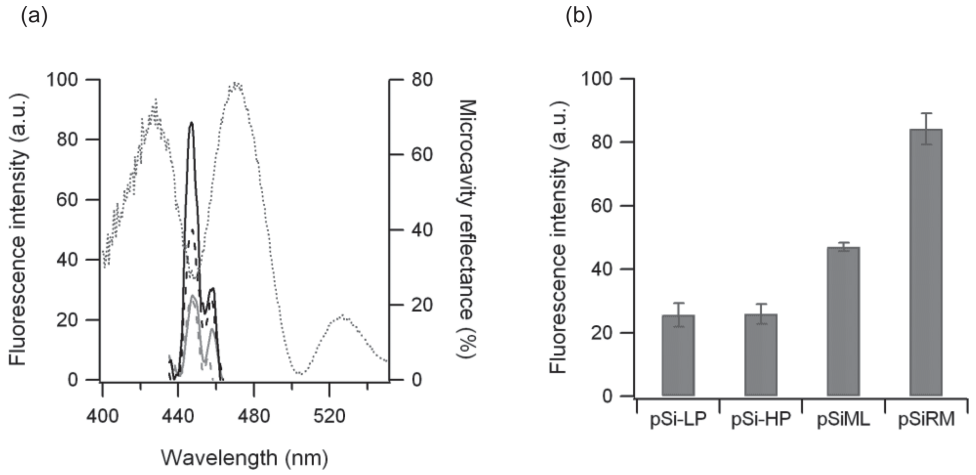

Figure 4. a) Fluorescence spectra of different pSi architectures: single layer pSi with low porosity (pSi-LP, grey dashed line), single layer pSi with high porosity (pSi-HP, grey full line), multilayer pSi with alternating HP and LP layers (pSiML with resonance at 446.5 nm, black dashed line) and pSiRM (black full line). The dotted line represents the reflectance spectrum of pSiRM. b) Emission intensities at 446.5 nm from four different pSi structures with the error bars calculated from three separate experiments.

2.3.3. Factors Affecting The Sensitivity of The pSiRM-Based Optical Biosensor

Our results so far demonstrate that the emission from the pSiRM is superior to emission in solution. We next investigated emission for different pSi architectures of identical thickness after incubation with MMP-1 (1.2×10^{-7} M) (**Figure 4**). All samples had undergone the same surface modification procedure resulting in surfaces displaying fluorogenic peptide (as confirmed by IR spectroscopy).

Figure 4a,b shows that the EDANS emission intensity of the fluorophore embedded in the pSiRM structure was about three times and two times higher compared to the single pSi layers (both HP and LP) and the pSi multilayer, respectively. This result confirms that the microcavity architecture is indeed able to enhance fluorescence emission[43] and that this platform may serve as a sensitive transducer for the presence of MMP-1 in solution.

We also investigated the effect of tuning the cavity to the emission wavelength of the fluorophore and compared two pSiRMs, one has a dip at 440 nm (designed at 432 nm) and the other at 500 nm (designed at 492 nm) after etching or before surface functionalization (**Figure 5**). The resonance of the freshly etched pSiRM at 440 nm, was shifted into 446.5 nm after surface modification, as explained above, giving a perfect match with the emission maximum of EDANS. The other pSiRM after surface modification gave a resonance peak at 506.7 nm, where EDANS embedded in the pSi layer does not have substantial emission.

Figure 5 shows that after incubation with MMP-1 (1.2×10^{-7} M), the emission intensity of the tuned pSiRM was about four times higher compared to the untuned one. This corroborates the point that optimal fluorescence is obtained when the wavelength of resonance cavity dip is tuned to the emission wavelength of fluorophore[43] and underscores that the resonance cavity layer is the sensitive part of the pSiRM.

We then shifted our attention to the porosity contrast between LP and HP layer since this determines the Q factor, which is often a predictor of the sensitivity in an optical biosensor.[35,36,40] The Q factor is defined as $Q = \lambda/\Delta\lambda$, where λ is the center wavelength of the resonance cavity dip and $\Delta\lambda$ is the full width at half maximum (FWHM) of the resonance cavity dip,[36,39,40] and indicates the effectiveness with which light is confined in the resonance cavity layer.[39] The Q factor can be increased by increasing the porosity contrast between LP and HP layers and also the number of periods in each DBR.

For the chosen configuration of $(HP/LP)_3(HP)_4(LP/HP)_3$, the porosity contrast was 16.4% and the reflectance spectrum (black trace in Figure 1a) gave a Q factor of 25 (measured at incident light 0°). There is no standard value of Q factor to produce a sensitive biosensor based on a pSiRM structure.[57] DeLouise et al. reported that the pSiRM with 20% porosity contrast had a Q factor of 28 for 5 periodic layer in the DBR and this value increased to 130 by doubling the number of periodic layer.[40] Palestino et al. showed that the pSiRM with 15% porosity contrast and the Q factor of 40–50 was sensitive enough to detect 1–2 nm shift of the resonance peak.[37] The Q factor of our pSiRM was slightly lower than that reported by DeLouise et al.

In order to investigate the influence of the Q factor value on sensor performance, we increased the porosity contrast and the number of periods in each DBR. Note that for a pSiRM structure with the same configuration of $(HP/LP)_3(HP)_4(LP/HP)_3$ but with a porosity contrast of 19.3% (86.3% for HP and 67% for LP) the Q factor increased to 44 (measured at incident light angle of 0°) and for a pSiRM structure with the same porosity contrast but having four periodic layers in each DBR $((HP/LP)_4(HP)_4(LP/HP)_4)$, the Q factor was 45 (again measured at incident light angle of 0°). We compared these three pSiRMs and observed that the pSiRM with a Q factor of 25 showed the highest EDANS emission intensity, producing a 4-fold and 8-fold higher signal than the pSiRMs with Q factors of 44 and 45, respectively, at the same concentration of MMP-1 (1.2×10^{-7} M) (see Supporting Information, Figure S2a).

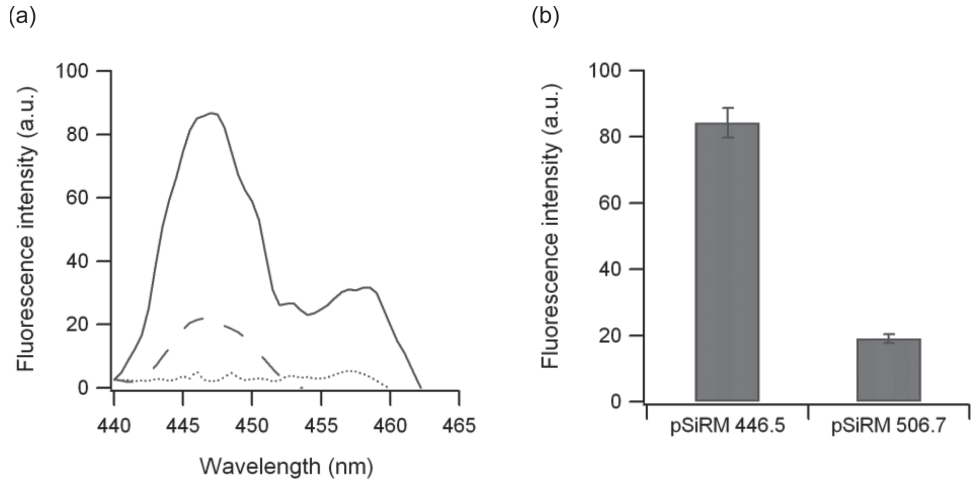

Figure 5. a) Comparison of fluorescence emission spectra observed at 446.5 nm from the pSiRMs with cavity dip at 446.5 nm (full line) and at 506.7 nm (dashed line) after incubation with MMP-1. The dotted line corresponds the control sample, which was not incubated with MMP-1. b) The emission intensity at 446.5 nm of both pSiRM with the error bars calculated from three separate experiments.

This finding shows that raising the *Q* factor by increasing the porosity contrast or the number of DBR periods did not translate into higher sensitivity in the biosensor (see Supporting Information, Figure S2b). We attribute this interesting phenomenon to two effects: MMP infiltration and light distribution throughout the pSiRM layers. With higher porosity contrast, the difference in pore size between LP and HP also increases, resulting in potential trapping of MMP in the LP layer. This may negatively impact on the ability of MMP to cleave the peptide within the defect layer of the pSiRM. For the thicker DBRs, the attenuation of excitation light at 340 nm becomes a problem since less light reaches the defect layer, reducing confined fluorescence emission. This effect is demonstrated in the simulation in Figure S3 (Supporting Information), where the electric field distribution of the thinner cavity (black trace) in the defect layer is higher than for the thicker cavity (grey trace).

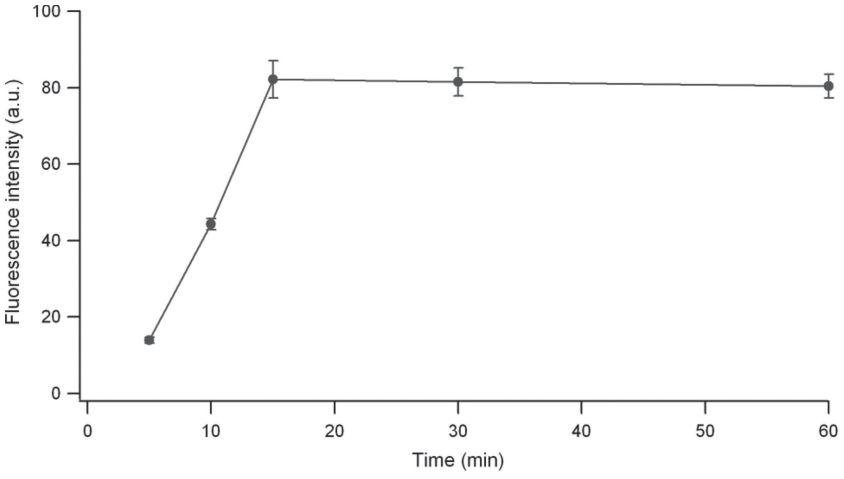

Figure 6. Fluorescence emission intensities for different incubation times. The error bars were calculated from three separate experiments.

2.3.4. Sensing Performance

In POC diagnostic devices, a short response time and a low detection limit are highly desirable. Therefore, both parameters were investigated here. We first studied the effect of incubation time with 1.2×10^{-7} M MMP-1 on fluorescence signal level using the peptide-functionalized pSiRM with the tuned cavity wavelength.

Figure 6 presents the EDANS fluorescence intensity at different incubation times. After 5 min of incubation, a significant fluorescence emission indicating the presence of MMP-1 was already detectable. The fluorescence intensity increased with increasing incubation time (due to increasing amounts of peptide cleavage) and then plateaued at 15 min incubation time (when apparently all fluorogenic peptide was cleaved). Therefore, 5 min of incubation time and a single incubation and washing step sufficed to generate a strong optical signal in response to MMP-1 solution, which is encouraging for a POC sensor.

The fluorescence emission intensity after incubation with different concentrations of MMP-1 (logarithmic scale) is shown in **Figure 7**. The optical signal increased linearly with increasing MMP-1 concentration from 10^{-7} M to 10^{-12} M (five orders of magnitude) with a linear regression equation of $y = 10.345x + 153.37$ ($R^2 = 0.99535$). At lower concentrations, the fluorescence intensity increased only gradually with increasing MMP-1 concentration. This effect was attributed to the diffusion of the small amount MMP-1 inside the cavity layer generated a preconcentration effect.[43] The lowest concentration of MMP-1 we attempted to detect was 2.4×10^{-18} M. However, to determine the limit of detection (LOD), we use the equation of

$$\mathrm{LOD} = y_b + 3\mathrm{Std}_b \quad (2)$$

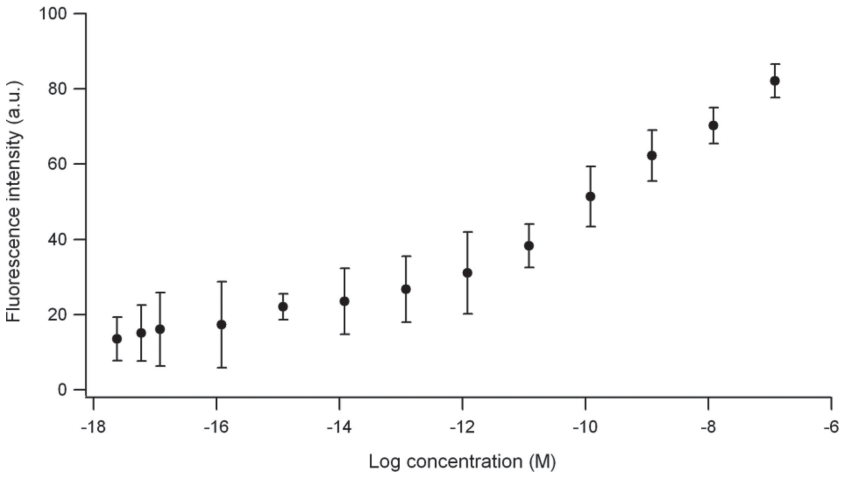

Figure 7. Fluorescence emission intensity of peptide-functionalized pSiRM after incubation with MMP-1 at different concentrations for 15 min. The error bars were calculated from the three separate experiments.

where γ_b is the concentration of blank (control solution in the absence of MMP-1) and Std_b is the standard deviation of blank. From this equation, the calculated LOD was 7.5×10^{-19} M.

To the best of our knowledge, this represents by far the most sensitive MMP biosensor for MMPs detection. Gogly et al. reported a detection limit as low as 2.4×10^{-15} M in the case of an MMP-1 assay on collagen zymograms.[58,59] Using surface plasmon resonance (SPR) Jung et al., were able to detect MMP-3 in the range of 9.3×10^{-10}–3.7×10^{-7} M.[60] A single-walled carbon nanotube based assay had a detection limit of 7.4×10^{-12} M for MMP-3.[61] The MMPs biosensor based on the pSiRM structure developed by Martin et al. which observing the shift of the cavity during sensing was able to detect as low as 1.5×10^{-9} M MMP-8.[21]

Considering the excellent sensitivity of our system, it may further be developed as a POC sensor. However as a POC, the sensing approach, especially rinsing and drying steps, may need to be modified without reducing the selectivity and sensitivity of the sensor. One possibility is by using a microfluidic channel which has a controllable diffusion to separate a binding molecule from unbinding molecules thus the rinsing and drying step can be omitted. Another possibility is by using a microfluidic channel equipped with a micropump and microvalve to control the rinsing process and the drying step may be done by pushing air through the channel.

2.4. Detection of MMP in Wound Fluid

Our peptide-functionalized pSiRM sensor detected MMP-1, as representative of MMPs, in buffer solution with excellent sensitivity. Following this, the same sensing platform was applied to detect MMPs in wound fluid, which contains a large number of biomolecules that could potentially interfere with the biosensor.[45,62–64] The wound fluid sample used in this study was human chronic wound fluid collected from six patients with chronic venous leg ulcers attending the multidisciplinary foot clinic at The Queen Elizabeth Hospital (South Australia, Australia).[23] Western Blot of this wound fluid (see supporting information, Figure S4) confirmed the presence of MMPs.[23]

Upon incubation of the peptide-functionalized pSiRM with a tuned cavity dip in wound fluid we observed a strong emission signal after 15 min, confirming the presence of MMPs in the wound fluid (**Figure 8**a). In order to determine potential matrix effects in wound fluid, the fluorescence intensity of the wound fluid sample spiked with the different concentration of MMP-1 (1.2×10^{-7} M, 1.2×10^{-8} M, 1.2×10^{-9} M, 1.2×10^{-10} M, 1.2×10^{-11} M, and 1.2×10^{-12} M) was determined. The signal generated from wound fluid sample containing MMP-1 produced a linear response with the linear regression equation of $y = 10.188x + 185.52$ ($R^2 = 0.99115$). Both calibration curves (Figure 8b), in buffer solution (taken from a linear range of Figure 7) and in wound fluid, gave a similar slope, demonstrating the absence of matrix effects. Using the standard addition approach, the signal from wound fluid in Figure 8a corresponds to 1.5×10^{-15} M. In order to study the possible impact of a large number biomolecules including protein in the wound fluid sample on the fluorescence signal, the fluorescence emission of the various concentration of neat dye in the presence and absence of the wound fluid were compared (see Supporting Information, Figure S5). The results showed that the presence of protein and other biomolecules in wound fluid sample only slightly decreased the fluorescence signals. Our results confirm that the emission signal of the pSiRM after incubation with wound fluid was due to the MMP-catalyzed cleavage of the immobilized fluorogenic

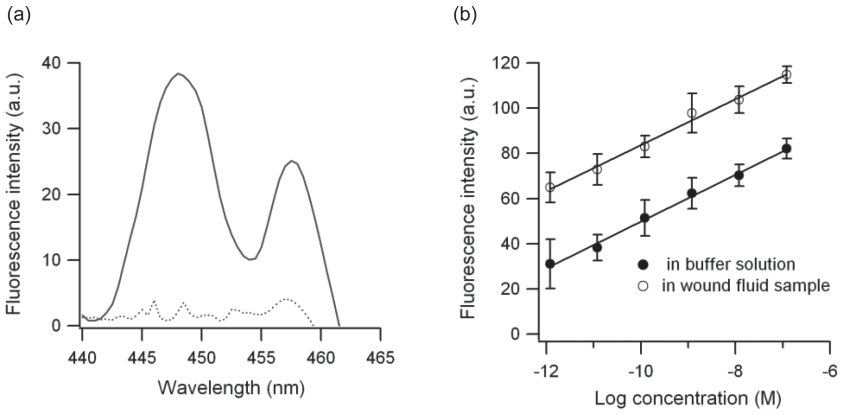

Figure 8. a) Fluorescence emission spectra of peptide-functionalized pSiRM after immersion in wound fluid (WF) (full line). The dotted line corresponds to the control pSiRM not incubated with wound fluid. b) Comparison of average emission intensity of different concentration of MMP-1 in buffer solution and spiked to wound fluid sample with error bars calculated from three separate experiments.

peptide substrate and that the presence of other molecules in the wound fluid did not cause significant interferences.

3. Conclusion

We present a fluorescence-based optical biosensor for MMP-1 based on a photonic pSiRM structure that was carefully designed by considering parameters such as pore size, porosity, Q factor, number of periods in the DBRs, the angle of the incident light and the corresponding wavelength of the photonic band gap. The pSiRM surface was functionalized with a fluorogenic peptide substrate for MMP as confirmed by FTIR-ATR spectra.

The EDANS emission observed in the pSiRM surface was stronger and narrower than the emission observed in solution at the same MMP-1 concentration, due to confinement and enhancement effects in the pSiRM, and also stronger compared to other pSi architectures such as single layer and multilayer. Tuning of the cavity position to the EDANS emission peak was found to be essential.

The presence of MMP-1 in buffer solution was detected after 5 min and a single incubation step. In addition, this sensor successfully detected MMP-1 with a limit of detection of 7.5×10^{-19} M. MMP detection was also achieved for human chronic wound fluid, which is the clinically relevant sample for this type of sensor. Thus, our results set the stage for the development of much needed POC biosensors that underpin improvements in the management of chronic wounds.

4. Experimental Section

Materials: All chemical and reagents were purchased from Sigma-Aldrich unless otherwise stated. High purity solvents (methanol, ethanol, acetone and dichloromethane) were purchased from Chem Supply. All pSi samples were prepared from highly doped, (100)- oriented, phosphorus doped n-type Si wafer (0.008 – 0.02 Ω cm, Siltronix). The Si wafer was diced using a diamond cutter into pieces of 3–4 cm^2.

Design, Fabrication and Characterization of pSiRM Samples: pSi samples were prepared in a Teflon-based electrochemical etching cell using an aluminium tape as a contact for the silicon piece as anode and a platinum mesh as cathode. The electrochemical etching solution contains 25:200:1 volume ratio of aqueous hydrofluoric acid (48%, Scharlau)/water/surfactant (NCW1001, Wako Pure Chemical Industries).[36] The Si wafer was pre-treated in order to remove the parasitic layer from the substrate by anodically etched Si wafer at a current density of 40 mA cm^{-2} for 30 s, followed by a current density of 250 mA cm^{-2} for 6 s which led to electropolishing. Following this step, the surface was exposed to MilliQ water for 1 min to remove the sacrificial layer, then rinsed with methanol, acetone, dichloromethane and dried under a stream of nitrogen gas. The pre-treated Si wafer was then etched for 2 min at current densities specified in Table S1 (Supporting Information) to fabricate single layer pSi films used during the design of the pSiRM. The single layer pSi samples were rinsed with methanol, acetone, dichloromethane and dried under a stream of nitrogen gas. The freshly etched single layer pSi samples were characterized using IRS, where a bifurcated optical fiber delivered tungsten light along the surface normal and collected reflected light into a CCD spectrometer. IRS was used to collect reflectance spectra of single layer pSi etched at different current densities.[46] By means of a simulation program (SCOUT, obtained from M. Theiss Hard- and Software), which is based on the transfer matrix method, the best fit between the experimental and theoretical reflectance spectrum was used to determine porosity and thickness value of single layer pSi films.[65] The pSiRM structure was then designed via the SCOUT program based on the obtained porosity and thickness values of the single layer pSi film. The contrast of porosity and thickness was chosen to obtain an appropriate refractive-index profile of the pSiRM with the position of the resonance cavity dip at the desired wavelength. The required current densities and etching time were also obtained via this method. The pSiRM samples were fabricated by anodically etching a Si wafer using a current density alternating between 50 mA cm^{-2} for 2288 ms and 25 mA cm^{-2} for 1820 ms corresponding to HP and LP layers, respectively. The defect layer was etched at a current density of 50 mA cm^{-2} for 9152 ms. The resulting pSiRM had the configuration $(HP/LP)_3(HP)_4(LP/HP)_3$. The pSiRM was also characterized using IRS to ensure that the reflectance spectrum matched that of the simulation. The single layer pSi and pSiRM samples were analyzed using SEM. A Quanta 450 field emission gun (FEG) Environmental SEM fitted with a Solid-State Detector (SSD) and an accelerating voltage of 30 kV was used.

Peptide Functionalization of pSiRM Samples: The freshly etched pSiRM samples were functionalized by thermal hydrosilylation of neat undecylenic acid in a glass reaction flask. Before performing the reaction, the undecylenic acid was purged with argon for 15 min to remove any oxygen. The pSiRM samples were then immersed in the undecylenic acid and purged for an additional 30 min. Afterwards, the reaction flask was immersed in an oil bath at 120 °C and the reaction proceeded for 3 h under an argon flow. Afterwards, the hydrosilylated pSiRM samples were removed from the flask, rinsed with ethanol and dried gently under a stream of nitrogen gas. The hydrosilylated pSiRM with a carboxylic acid-terminated surface was activated to form NHS ester-terminated surface by reacting the pSiRM samples with N-hydroxysuccinimide (NHS) (5 mM) in water in the presence of 1-(3-dimethylaminopropyl)-3-ethylcarbodiimide (EDC, Fluka) (5 mM) for 20 min at room temperature. The samples were then rinsed with water and dried gently under a stream of nitrogen gas. Immobilization of the fluorogenic MMP peptide substrate Dabcyl-Gaba-Pro-Gln-Gly-Leu-Glu(EDANS)-Ala-Lys-NH_2, (Merck) was carried out by overnight incubation of the functionalized pSiRM surface with peptide (10 mM) in a buffer solution prepared from Trizma Base (50 mM, pH 7.6), sodium chloride (NaCl, Chem Supply) (150 mM), calcium chloride dehydrate ($CaCl_2 \cdot 2H_2O$, Ajax Chemical Ltd.) (5 mM), zinc chloride ($ZnCl_2$, Merck) (1 μM) and 0.01% Brij L23.[11,19] Afterwards, the surface was rinsed with water, 2:1 water/ethanol, 1:2 water/ethanol and ethanol. Finally, the pSiRM surface was dried gently under a stream of nitrogen gas. This modified pSiRM surface was then ready for use in biosensing experiments.

FTIR Spectroscopy: FTIR analysis was conducted after each step of the surface functionalization procedure. FTIR spectra were obtained using a Vertex 70 Hyperion microscope (Bruker) in the ATR mode. Background spectra were taken in air and sample spectra recorded over the range 650–4000 cm^{-1}, at a resolution of 22 cm^{-1}, an aperture size of 3 mm and averaging 64 scans. The base line was corrected and normalized with OPUS 7.2 Spectroscopy Software (Bruker). All samples for FTIR analysis were prepared from p-type Si wafer with a resistivity of 0.00055–0.001 Ω cm etched at current density 56 mA cm^{-2} for 2 min.

Biosensor Experiments: Prior to use in the biosensor experiments, Recombinant human MMP-1 (R&D Systems) was activated using previously published procedure.[11,12] Briefly, freshly prepared 4-aminophenylmercuric acid (APMA, Aldrich) (100 mM) in dimethyl sulfoxide (Sigma-Aldrich) was added to recombinant human MMP-1 to give a final APMA concentration of 1 mM followed by the incubation at 37 °C for 3 h. The peptide functionalized pSiRMs were incubated in activated MMP-1 at varying concentrations at 37 °C for a few min and then rinsed with water, 2:1 water/ethanol, 1:2 water/ethanol and ethanol to remove unbound analytes. Afterwards, the samples were dried gently under a stream of nitrogen gas. The dried pSiRM surface was placed in a cuvette with a special holder to support the pSiRM film. The cuvette was then placed in a fluorometer with the position of pSiRM surface facing the light source at a 36° angle. Finally, the fluorescence intensity of the fluorophore (EDANS) was measured

using a fluorometer (Parkin Elmer LS 55 Luminescence Spectrometer). The emission was measured over a wavelength range of 360–540 nm at a fixed excitation wavelength of 340 nm, excitation and emission slit widths of 5 nm each and a scan speed of 200 nm min^{-1}. The angle formed by the light source of the fluorometer and the defect layer of the pSiRM in respect to the surface normal was set to 36° since we obtained highest fluorescence signals at this angle. Human wound fluid sample was collected from Women's and Children's Hospital (Adelaide, South Australia). The study protocol, which conformed to the ethical guidelines of the 1975 Declaration of Helsinki, was approved by the Health Service Human Research Ethics Committee and Central Northern Adelaide Health Service Ethics of Human Research Committee. The wound fluid was diluted 10-fold in buffer solution. The sensing platform was incubated in the wound fluid sample at 37 °C and then treated in the same ways as described above.

Supporting Information

Supporting Information is available from the Wiley Online Library or from the author.

Acknowledgements

The authors thank Allison Cowin and Elizabeth Melville from Mawson Institute for providing the wound fluid sample, Beatriz Prieto Simón and Martin Sweetman for useful discussions, the Wound Management Innovation CRC for providing funding for this work, and the Mawson Institute and International President's Scholarship (IPS) for a PhD scholarship for F.S.H.K.

Received: December 3, 2013
Revised: January 19, 2014
Published online: March 3, 2014

[1] K. Harding, Principles of Best Practice: Diagnostics and Wounds A concensus Document, London, **2007**.
[2] T. R. Dargaville, B. L. Farrugia, J. A. Broadbent, S. Pace, Z. Upton, N. H. Voelcker, *Biosens. Bioelectron.* **2013**, *41*, 30.
[3] H. Brem, O. Stojadinovic, R. F. Diegelmann, H. Entero, B. Lee, I. Pastar, M. Golinko, H. Rosenberg, M. Tomic-Canic, *Mol. Med.* **2007**, *13*, 30.
[4] C. K. Sen, G. M. Gordillo, S. Roy, R. Kirsner, L. Lambert, T. K. Hunt, F. Gottrup, G. C. Gurtner, M. T. Longaker, *Wound Rep. Reg.* **2009**, *17*, 763.
[5] T. Velnar, T. Bailey, V. Smrkolj, *J. Int. Med. Res.* **2009**, *37*, 1528.
[6] N. Mehmood, A. Hariz, R. Fitridge, N. H. Voelcker, *J. Biomed. Mater. Res., Part B* **2013**, *00B*, 000.
[7] N. T. Thet, S. H. Hong, S. Marshall, M. Laabei, A. Toby, A. Jenkins, *Biosens. Bioelectron.* **2013**, *41*, 538.
[8] J. Zhou, A. L. Loftus, G. Mulley, A. T. A. Jenkins, *J. Am. Chem. Soc.* **2010**, *132*, 6566.
[9] J. Zhou, T. N. Tun, S.-h. Hong, J. D. Mercer-Chalmers, M. Laabei, A. E. R. Young, A. T. A. Jenkins, *Biosens. Bioelectron.* **2011**, *30*, 67.
[10] K. G. Harding, H. L. Morris, G. K. Patel, *BMJ* **2002**, *324*, 160.
[11] Y. Cao, T. I. Croll, S. C. Rizzi, G. K. Shooter, H. Edwards, K. Finlayson, Z. Upton, T. R. Dargaville, *J. Biomed. Mater. Res.* **2011**, *96A*, 663.
[12] W. Bode, C. Fernandez-Catalan, H. Tschesche, F. Grams, H. Nagase, K. Maskos, *Cell. Mol. Life Sci.* **1999**, *55*, 639.
[13] J. L. Gorman, E. Ispanovic, T. L. Haas, *Drug Discovery Today: Dis. Models* **2011**, *8*, 5.
[14] R. Visse, H. Nagase, *Circ. Res.* **2003**, *92*, 827.
[15] R. P. Verma, C. Hansch, *Bioorganic and Medicinal Chemistry* **2007**, *15*, 2223.
[16] N. J. Trengove, M. C. Stacey, S. Macauley, N. Bennett, J. Gibson, F. Burslem, G. Murphy, G. Schultz, *Wound Rep. Reg.* **1999**, *7*, 442.
[17] J. F. Woessner, *FASEB J.* **1991**, *5*, 2145.
[18] H. F. Bigg, A. D. Rowan, *Curr. Opin. Pharmacol.* **2001**, *1*, 314.
[19] B. Beekman, J. W. Drijfhout, W. Bloemhoff, H. K. Ronday, P. P. Tak, J. M. te Koppele, *FEBS Lett.* **1996**, *390*, 221.
[20] L. Gao, N. Mbonu, L. Cao, D. Gao, *Anal. Chem.* **2008**, *80*, 1468.
[21] M. Martin, C. T. Bendiab, L. Massif, G. Palestino, V. Agarwal, F. Cuisinier, C. Gergely, *Phys. Status Solidi C* **2010**, 1.
[22] K. A. Kilian, L. M. H. Lai, A. Magenau, S. Cartland, K. Gaus, J. J. Gooding, *Nanoletters* **2009**, *9*, 2021.
[23] F. S. H. Krismastuti, A. J. Cowin, S. Pace, E. Melville, T. R. Dargaville, N. H. Voelcker, *Aust. J. Chem.* **2013**.
[24] A. Jane, R. Dronov, A. Hodges, N. H. Voelcker, *Trends Biotechnol.* **2009**, *27*, 230.
[25] H. Ouyang, C. C. Striemer, P. M. Fauchet, *Appl. Phys. Lett.* **2006**, *88*, 1631081.
[26] H. Ouyang, L. A. DeLouise, B. L. Miller, P. M. Fauchet, *Anal. Chem.* **2007**, *79*, 1502.
[27] E. J. Anglin, L. Cheng, W. R. Freeman, M. J. Sailor, *Adv. Drug Delivery Rev.* **2008**, *60*, 1266.
[28] S. P. Low, N. H. Voelcker, L. T. Canham, K. A. Williams, *Biomaterials* **2009**, *30*, 2873.
[29] M. Arroyo-Hernandez, R. J. Martin-Palma, J. Perez-Rigueiro, J. P. Garcia-Ruiz, J. L. Garcia-Fierro, J. M. Martinez-Duart, *Mater. Sci. Eng., C* **2003**, *23*, 697.
[30] B. Guan, A. Magenau, K. A. Kilian, S. Ciampi, K. Gaus, P. J. Reece, J. J. Gooding, *Faraday Discuss.* **2011**, *149*, 301.
[31] K. A. Kilian, T. Bocking, J. J. Gooding, *Chem. Commun.* **2009**, 630.
[32] T. C. Do, H. Bui, T. V. Nguyen, T. A. Nguyen, *Adv. Nat. Sci.: Nanosci. Nanotechnol.* **2011**, *2*, 035001.
[33] S. Li, J. Huang, L. Cai, *Nanotechnology* **2011**, *22*, 425502 (6pp).
[34] L. De Stefano, I. Rendina, L. Moretti, S. Tundo, A. M. Rossi, *Applied Optics* **2004**, 43.
[35] G. Palestino, V. Agarwal, D. B. Garcia, R. Legros, E. Perez, C. Gergely, Optical Characterization of Porous Silicon Microcavities for Glucose Oxidase Biosensing Vol. 6991 (Eds.: J. Popp, W. Drexler, V. V. Tuchin, D. L. Matthews), SPIE, **2008**, pp. 69911Y.
[36] H. Ouyang, M. Christophersen, R. Viard, B. L. Miller, P. M. Fauchet, *Adv. Funct. Mater.* **2005**, *15*, 1851.
[37] G. Palestino, V. Agarwal, R. Aulombard, E. Perez, C. Gergely, *Langmuir* **2008**, *24*, 13765.
[38] L. De Stefano, L. Rotiroti, E. De Tommasi, I. Rea, I. Rendina, M. Canciello, G. Maglio, R. Palumbo, *J. Appl. Phys.* **2009**, *106*, 0023109.
[39] L. A. DeLouise, P. M. Fauchet, B. L. Miller, A. A. Pentland, *Adv. Mater.* **2005**, *17*, 2199.
[40] L. A. DeLouise, P. M. Kou, B. L. Miller, *Anal. Chem.* **2005**, *77*, 3222.
[41] S. Chan, S. R. Horner, P. M. Fauchet, B. L. Miller, *J. Am. Chem. Soc.* **2001**, *123*, 11797.
[42] S. Chan, Y. Li, L. J. Rothberg, B. L. Miller, P. M. Fauchet, *Mater. Sci. Eng., C* **2001**, *15*, 277.
[43] B. Sciacca, F. Frascella, A. Venturello, P. Rivolo, E. Descrovi, F. Giorgis, F. Geobaldo, *Sens. Actuators, B* **2009**, *137*, 467.
[44] S. Iyer, R. Visse, H. Nagase, K. R. Archarya, *Jornal of Molecular Biology* **2006**, *362*, 78.
[45] D. Hanson, D. Langemo, P. Thompson, J. Anderson, S. Hunter, *Advances in Skin and Wound Care* **2005**, *18*, 360.
[46] S. Pace, R. B. Vasani, F. Cunin, N. H. Voelcker, *New J. Chem.* **2013**, *37*, 228.

[47] V. S.-Y. Lin, K. Motesharei, K. Dancil, M. J. Sailor, M. R. Ghadiri, *Science* **1997**, *278*, 840.
[48] C. Pacholski, M. Sartor, M. J. Sailor, F. Cunin, G. M. Miskelly, *J. Am. Chem. Soc.* **2005**, *127*, 11636.
[49] T. Bocking, K. A. Kilian, K. Gaus, J. J. Gooding, *Adv. Funct. Mater.* **2008**, *18*, 3827.
[50] R. Boukherroub, J. T. C. Wojtyk, D. D. M. Wayner, D. J. Lockwood, *J. Electrochem. Soc.* **2002**, *149*, H59.
[51] S. Sam, L. Touahir, J. Salvador Andresa, P. Allongue, J. N. Chazalviel, A. C. Gouget-Laemmel, C. Henry de Villenueve, A. Moraillon, F. Ozanam, N. Gabouze, S. Djebbar, *Langmuir* **2009**, *26*, 809.
[52] B. Sciacca, E. Secret, S. Pace, P. Gonzalez, F. Geobaldo, F. Quignard, F. Cunin, *J. Mater. Chem.* **2011**, *21*, 2294.
[53] T. Bocking, E. L. S. Wong, M. James, J. A. Watson, C. L. Brown, T. C. Chilcott, K. D. Barrow, H. G. L. Coster, *Thin Solid Films* **2006**, *515*, 1857.
[54] B. A. Mast, G. S. Schultz, *Wound Rep. Reg.* **1996**, *4*, 411.
[55] U. K. Saarialho-Kere, *Arch. Dermatol. Res.* **1998**, *290*, S47.
[56] A. Venturello, C. Ricciardi, F. Giorgis, S. Strola, G. P. Salvador, E. Garrone, F. Geobaldo, *J. Non-Cryst. Solids* **2006**, *352*, 1230.
[57] H. Ouyang, P. M. Fauchet, *Proc. of The SPIE Conference*, Boston **October 2005**.
[58] B. Gogly, N. Groult, W. Hornebeck, G. Godeau, B. Pellat, *Anal. Biochem* **1997**, *255*, 211.
[59] C. Lombard, J. Saulnier, J. Wallach, *Biochemie* **2005**, *87*, 265.
[60] S.-H. Jung, D.-H. Kong, J. H. Park, S.-T. Lee, J. Hyun, Y.-M. Kim, K.-S. Ha, *Analyst* **2010**, *135*, 1050.
[61] B. S. Munge, J. Fisher, L. N. Millord, C. E. Krause, R. S. Dowd, J. F. Rusling, *Analyst* **2010**, *135*, 1345.
[62] S. A. Eming, M. Koch, A. Krieger, B. Brachvogel, S. Kreft, L. Bruckner-Tuderman, T. Krieg, J. D. Shannon, J. W. Fox, *J. Proteome Res.* **2010**, *9*, 4758.
[63] R. W. Tarnuzzer, G. S. Schultz, *Wound Rep. Reg.* **1996**, *4*, 321.
[64] D. R. Yager, B. C. Nwomeh, *Wound Rep. Reg.* **1999**, *7*, 433.
[65] M. Born, E. Wolf, Principles of Optics: Electromagnetic Theory of Propagation, Interference and Diffraction of Light seventh ed., Cambridge University Press, New York, **1999**.